Stress results from two-dimensional granular shear flow simulations using various collision models

William R. Ketterhagen,[1] Jennifer S. Curtis,[2] and Carl R. Wassgren[3,*]
[1]*School of Chemical Engineering, Purdue University, West Lafayette, Indiana 47907, USA*
[2]*Chemical Engineering Department, University of Florida, Gainesville, Florida 32611, USA*
[3]*School of Mechanical Engineering, Purdue University, West Lafayette, Indiana 47907, USA*
(Received 5 August 2004; revised manuscript received 26 April 2005; published 30 June 2005)

Collision resolution is one of the key elements in a discrete element method algorithm for modeling granular flows. Several collision models have been proposed for this process. The hard-particle collision approach is typically used for dilute systems, or for those in which the assumption of binary and instantaneous particle-particle contact remains valid. As the solids fraction increases, however, multiple, enduring collisions can occur and a soft-particle approach is more appropriate for resolving the collision dynamics. In this work, the delineation between dilute and dense systems and the suitability of contact models are explored for a range of solid fractions. Stress results for two-dimensional shear flow simulations are compared using several collision models including an event-driven hard-particle model, a hysteretic spring soft-particle collision model following Walton and Braun [J. Rheol. **30**, 949 (1986)], and a hybrid hard-particle-with-overlap model following Hopkins and Louge [Phys. Fluids A **3**, 47 (1991)]. Results show that stresses are accurately predicted for a range of solids fractions, coefficients of restitution, and friction coefficients by both the hard-particle-with-overlap and soft-particle models so long as a sufficiently large loading stiffness is used for the soft-particle model. Additional results investigating the accuracy of the collision models and the amount of collisional overlap are presented as functions of the simulation time step and model parameters.

DOI: 10.1103/PhysRevE.71.061307 PACS number(s): 45.70.−n, 02.70.Ns, 45.05.+x, 83.80.Fg

I. INTRODUCTION

The flow of granular materials has been the subject of considerable study. Shear flow of granular materials provides a convenient and relatively simple starting point for understanding fundamental flow behavior. These flows are often studied experimentally using an apparatus such as an inclined chute or a Couette flow device, or with computational approaches such as the discrete element method (DEM). The use of the DEM approach as applied to simple shear flow and the required model parameters are the subject of the current work.

Experimental studies of dilute granular shear flows have been performed using an inclined chute for making measurements of particle translational and rotational velocities in rapid, quasi-two-dimensional (quasi-2D) flow [1]. For dense systems, a Couette geometry is often used to measure particle velocities, velocity fluctuations, and packing densities [2–4]. A Couette geometry has also been used to measure particle velocities and shear stress for the intermediate regime between the dilute and dense limits [5].

Several researchers have also compared computational results with experimental results. For example, Drake and Walton [6] found good agreement between simulation results and experimentally measured particle translational and rotational velocities, velocity fluctuations, and bulk density for dilute chute flow. Also, Lätzel *et al.* [7] drew comparisons between computational and experimental results for dense 2D Couette flow. In their work, good quantitative agreement for the bulk density and a qualitative agreement for the velocity profiles were reported.

In addition to these experimental approaches, modeling granular flows using the DEM has become a common technique in efforts to better understand systems of granular materials. An inherent benefit of these simulations is that the state of every particle is known at all times. While this information can have a high computational cost for very large systems, it does allow for the measurement of many system quantities of interest. For instance, velocity profiles, local solids fraction, granular temperature, and the stress tensor are all readily determined from particle state information. The stress tensor is often reported in two-dimensional (see, for example, [8–10]) and three-dimensional (see, for example, [11]) shear flows. Stress tensor measurements allow for a relatively straightforward comparison between simulations of different systems and with different computational algorithms, as well as with kinetic theories.

At the heart of a DEM simulation is a particle interaction model. Upon detection of a particle contact, this particle interaction model is used to calculate the postcollision velocities of the colliding particles. There are two common techniques used to make this calculation, which are referred to as the hard- and soft-particle approaches.

The hard-particle approach assumes that particles are rigid so that collisions are instantaneous and binary. As a result, hard-particle models are generally best suited for dilute, collisional flows where these assumptions are good approximations. Hard-particle models often are embedded in event-driven collision detection schemes that increment the simulation time from one collision to the next. Consequently, hard-particle, event-driven simulations can be computationally efficient when the time between particle collisions is large.

*Author to whom correspondence should be addressed. Email address: wassgren@purdue.edu

The hard-particle model has often been used in simple shear simulations. Campbell and Brennen [12] used the model to measure the velocity, density, and granular temperature distributions for two-dimensional Couette flows. These simulations showed the formation of a layered microstructure at high solids fractions. Similar work by Campbell and Gong [8] examined the stress tensor in this system in two dimensions. This work was subsequently extended to study the stress in three-dimensional systems [11]. Each of these studies presented stress results and showed normal stress differences owing to anisotropies in the granular temperature. Liss and Glasser [13] have shown that the system stresses increase with system size to an asymptotic value which was attributed to inelastic microstructure formation. However, Lasinski *et al.* [14], have observed an increase in the stresses beyond these asymptotic values for larger systems in 3D. This secondary increase is attributed to larger scale banding and clustering phenomena similar to that seen in the 2D work of Tan and Goldhirsch [15] and Hopkins and Louge [9].

The soft-particle approach [16], on the other hand, relies on a force-displacement (and/or force-displacement rate) relation to determine the interaction between particles. The soft-particle method is not limited by the instantaneous contact time assumption and can be used to investigate long-lasting and multiple particle contacts. This approach proceeds via small time steps and is thus referred to as being time driven. Accurate integration of the resulting particle equations of motion dictates a small simulation time step and, hence, long computation times. Soft-particle methods are generally utilized for dense, enduring-contact flows.

The soft-particle approach has also been used to obtain stress results in various flow systems. Walton and Braun [10] examined stresses in a two-dimensional shear flow for a system of 30 disks as a function of shear rate, solids fraction, friction, and elasticity. Normal stress differences were present, especially for highly inelastic particles and low solids fractions. Babić *et al.* [17] further examined the stress tensor at high concentrations in two-dimensional systems, and showed that as the concentration increased from dilute to dense, the system transitioned from a rapid-flow to a quasistatic regime. However, this transition is not a sharp transition, and consists of two zones: a collisional zone at concentrations just smaller than the phase change transition point and a quasistatic zone just larger than this phase transition point. The collisional zone is characterized by the formation of force chains which increase the stress values. With increasing concentration, these force chains become more frequent and enduring. In the quasistatic zone, Babić *et al.* [17] report that force chains are present and that shear flow is maintained through particle rolling within a narrow shear band. Campbell [18] continued with this theme by studying the stresses in three-dimensional shear flows of frictional particles at very high solids fractions such that enduring, elastic particle contacts are prevalent. Campbell identified two regimes in this dense limit: the elastic-inertial regime in which the stresses scale with both elastic and inertial properties, and the elastic-quasistatic regime in which the stresses scale solely with elastic properties. The two different scalings dictate that the stresses may be made dimensionless in one of two ways. To scale with inertial properties, the stresses are normalized by dividing by $\rho d^2 \dot{\gamma}^2$, where ρ is the particle density, d is the particle diameter, and $\dot{\gamma}$ is the shear rate, while scaling with elastic properties, in 3D, the stresses are multiplied by d/k_L, where k_L is the contact stiffness. In 2D, one would simply divide the stresses by the contact stiffness k_L. Campbell concluded that at such large solids fractions, the granular matter becomes susceptible to instabilities, which cause the formation of force chains resulting in localized stresses that can vary by several orders of magnitude.

Hopkins [19] developed another particle interaction algorithm, one that is a hybrid of the event-driven hard-particle and the time-driven soft-particle models. The algorithm proceeds via small time steps as in the soft-particle approach, but particle collisions are resolved using the equations of the hard-particle collision model. This approach is referred to as the hard-particle-with-overlap model. Hopkins and Louge [9] used this approach in their study of microstructure formation and its effects on the stresses in a two-dimensional shear flow system. These stress results were in fairly good agreement with previous work which used the event-driven, hard-particle approach [8]. Additionally, Louge [20] used this approach to investigate the effects of frictional boundaries on three-dimensional, shearing flows.

Obviously, one would prefer to use the most accurate and computationally efficient models; however, the conditions separating the regimes where hard- and soft-particle models are best suited remains unclear. Furthermore, few studies [21] have compared results from hard- and soft-particle simulations of the same system to determine if the results exhibit model dependence. Additionally, aside from a few studies (see, for example, [17,18]), a large portion of DEM work does not show the dependence of results on model parameters such as spring stiffness and, in fact, the selection of these model parameters often appears to be rather arbitrary. This paper presents stress measurements for a granular shear flow using three common DEM computational modeling techniques: the event-driven hard-particle, the hard-particle-with-overlap, and the soft-particle methods. These results are also compared with kinetic theory predictions. The results are compared at various solids fractions, coefficients of restitution, and friction coefficients. Additionally, the dependence of the stress results on model parameters including spring stiffness and time step size is also examined.

II. COMPUTATIONAL MODELS

Three DEM models are utilized in this study to model a two-dimensional granular shear flow. The system consists of N identical, inelastic, frictionless (frictional in Sec. III C only) disks of diameter d and density $\rho = 4m/\pi d^2$, where m is the disk mass per unit length. The disks are placed in a square workspace of side length L, with the quantities L and d selected such that $L/d = 21$. The effect of L/d on the system stresses has been studied previously (see, for example, [9,13,14]); however, in the present work, the system size is set to $L/d = 21$ to maintain reasonable computational times

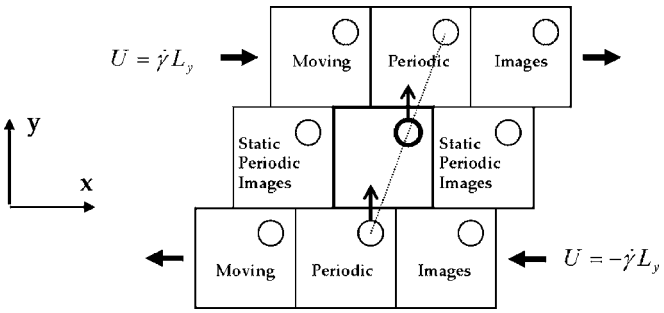

FIG. 1. A schematic of the simulated workspace.

while still using a statistically significant number of particles. No external forces are present and no interstitial fluid effects are considered. The horizontal x boundaries are periodic while the vertical y boundaries utilize Lees-Edwards periodic boundaries [22] that shear the assembly at a shear rate $\dot{\gamma}$. A schematic of the system is shown in Fig. 1. Particles are initially placed in the workspace at random positions, but with the assembly center of mass corresponding to the geometric workspace center. The particles are given an initial x velocity randomly distributed about a uniform shear flow profile while the initial y velocity is randomly distributed about a zero net y velocity. The net initial momentum of the system is zero.

Measurements of the system stress tensor are made by calculating the sum of the kinetic and collisional contributions as described by Campbell and Gong [8]. The kinetic stress $\boldsymbol{\tau}_{\mathbf{k}}$ is given by

$$\boldsymbol{\tau}_{\mathbf{k}} = \rho \nu \langle \mathbf{CC} \rangle, \tag{1}$$

where ν is the solids fraction within the system and $\mathbf{C} = \mathbf{c}_i - \langle \mathbf{c} \rangle$ is the fluctuating velocity of particle i. The average velocity $\langle \mathbf{c} \rangle$ is the steady-state, shear velocity profile. The collisional stress $\boldsymbol{\tau}_{\mathbf{c}}$ is given by

$$\boldsymbol{\tau}_c = \frac{d}{\Theta L^2} \sum_{\text{collisions}} \mathbf{J}\hat{\mathbf{n}}, \tag{2}$$

where Θ is the total simulated time after the initial transients, $\mathbf{J}$ is a collision impulse vector, and $\hat{\mathbf{n}}$ is the unit vector pointing from the center of particle i to the center of particle j. The stresses are made dimensionless by the quantity $\rho d^2 \dot{\gamma}^2$. After the initial transients, which have a duration of approximately 500 to 2500 collisions per particle, two averaging calculations for each stress component are made. An "instantaneous," or window, average is computed for a window size of 50 to over 500 collisions per particle for the largest solids fractions. Additionally, a running average of each stress component is computed. With these two averages, the point at which each component has reached a statistically steady value is determined, and the steady-state measurements are recorded.

Three collision evaluation algorithms are implemented in the simulations. These include the hard-particle, event-driven, the hard-particle-with-overlap, and the soft-particle approaches. A brief description of each approach is given below. More detail on the simulation algorithms can be found in the references cited in the introduction.

A. Hard-particle event-driven algorithm

The hard-particle collision model uses momentum conservation laws and the definition of the coefficient of normal and tangential restitution, e_N and e_S, respectively, to determine the states of particles after a collision. The momentum impulse $\mathbf{J}$ acting on particle i during a collision with particle j is given by

$$\mathbf{J} = \frac{1}{2} m (1 + e_N)(\mathbf{g} \cdot \hat{\mathbf{n}})\hat{\mathbf{n}} + \frac{1}{2} m \left(\frac{q}{q+1} \right)(1 + e_S)[\mathbf{g} - \hat{\mathbf{n}}(\mathbf{g} \cdot \hat{\mathbf{n}})], \tag{3}$$

where m is the particle mass (recall that the particles are assumed identical), $\mathbf{g}$ is the velocity of particle j relative to particle i at the point of contact, $\hat{\mathbf{n}}$ is the unit vector pointing from the center of particle i to the center of particle j, and q is a dimensionless constant related to the moment of inertia ($q = \frac{1}{2}$ for a cylinder). The tangential coefficient of restitution, defined by

$$e_S = -\frac{[\mathbf{g}^* - \hat{\mathbf{n}}(\mathbf{g}^* \cdot \hat{\mathbf{n}})]}{[\mathbf{g} - \hat{\mathbf{n}}(\mathbf{g} \cdot \hat{\mathbf{n}})]} \tag{4}$$

(where the asterisk denotes a postcollision quantity), relates the friction coefficient μ, the rolling tangential coefficient e_{S0}, and the tangential coefficient e_S as

$$e_S = \min \left[\mu (1 + e_N) \left(\frac{q+1}{q} \right) \frac{\mathbf{g} \cdot \hat{\mathbf{n}}}{\mathbf{g} - \hat{\mathbf{n}}(\mathbf{g} \cdot \hat{\mathbf{n}})} - 1, e_{S0} \right]. \tag{5}$$

The range of the tangential coefficient is $-1 \leqslant e_S \leqslant 1$, with $e_S = -1, e_S = 0$, and $e_S = 1$ corresponding to frictionless, no-slip, and perfectly elastic tangential rebound contacts, respectively. Thus, for frictionless particles, $\mu = 0$ and $e_S = -1$, and so Eq. (3) simplifies to

$$\mathbf{J} = \tfrac{1}{2} m (1 + e_N)(\mathbf{g} \cdot \hat{\mathbf{n}})\hat{\mathbf{n}}. \tag{6}$$

The translational and rotational velocities $\mathbf{c}$ and $\boldsymbol{\omega}$ respectively, of particle i after the collision are given by

$$\mathbf{c}_i^* = \mathbf{c}_i + \mathbf{J}/m, \tag{7}$$

$$\boldsymbol{\omega}_i^* = \boldsymbol{\omega}_i + \frac{-d(\hat{\mathbf{n}} \times \mathbf{J})}{2I}, \tag{8}$$

where $I = md^2/8$ is the moment of inertia for a disk. Following a collision, the times at which all future collisions occur are determined given the current particle states, the simulation advances to the next collision time, and the process repeats. This is known as an *event-driven* approach since the simulation increments from collision event to collision event rather than incrementing at a specified time step.

B. Hard-particle-with-overlap algorithm

The hard-particle-with-overlap model, originally developed by Hopkins [19], uses the hard-particle collision model

[Eqs. (3)–(8)], but integrates the particle equations of motion between collisions at a specified time step. This *time-driven* approach can be computationally more efficient than the event-driven approach for systems containing many particles. Proceeding at a specified time step, however, results in the possibility of particles overlapping prior to implementing the hard-particle collision model. As the simulation time step decreases, the particle overlap also decreases and, in the limit of infinitesimal time step, the hard-particle-with-overlap model results approach the event-driven hard-particle results.

C. Soft-particle algorithm

In the soft-particle approach the particle equations of motion are integrated in time just as with the hard-particle-with-overlap algorithm. However, in the soft-particle approach the interaction between particles is specified using a force-displacement relationship (sometimes displacement rate is also incorporated). A number of force-displacement models have been used in recent work, and have been reviewed by Schäfer *et al.* [23], Luding [24], and Herrmann and Luding [25]. The widely used hysteretic spring normal contact force model originally developed by Walton and Braun [10] is implemented here. The normal force during a contact, $\mathbf{F}_N$, is modeled using a linear spring during loading, and another stiffer, linear spring during unloading:

$$\mathbf{F}_N = \begin{cases} k_L \delta \hat{\mathbf{n}} & \text{for loading} \\ k_U(\delta - \delta_0)\hat{\mathbf{n}} & \text{for unloading,} \end{cases} \tag{9}$$

where k_L and k_U are the loading and unloading spring constants, respectively, δ is the overlap between particles, and δ_0 is the overlap at which the unloading force is zero due to plastic deformation of the particles. The effective coefficient of restitution for the contact is given by

$$e_N = \sqrt{\frac{k_L}{k_U.}} \tag{10}$$

Note that using Eq. (10) facilitates the comparison between the hard- and soft-particle models; however, Eq. (10) only specifies the ratio of the spring constants and not their magnitude. The dependence of the stresses on the magnitude of the spring constants is addressed in the following section. The tangential force $\mathbf{F}_S$ is modeled by Coulombic sliding friction,

$$\mathbf{F}_S = -\mu|\mathbf{F}_N|\hat{\mathbf{s}}, \tag{11}$$

where $\hat{\mathbf{s}}$ is the unit tangential vector pointing in the direction of the tangential relative velocity.

Most of the present work has considered frictionless disks, and thus investigates only the effects of the normal contact models on the measured stress. By considering only the normal interactions, the model parameters can be clearly be set to yield the same conditions through Eq. (10). However, the effect of friction has also been briefly examined in Sec. III C. For the frictional cases, the collision models were modified so that Coulombic frictional forces were modeled in the tangential direction. Elastic tangential forces (i.e., those modeled by a tangential spring) have not been considered because it is difficult to directly relate the effects of the hard-particle model's tangential restitution and the soft-particle model's tangential spring. Furthermore, some previous work has used similar Coulombic friction models for tangential forces (see, for example, [26–28]).

Prior to compilation of the current stress results, the simulation code was validated by running simulations for the same conditions as those used by previous researchers. The hard-particle-with-overlap model was validated with the results of Hopkins and Louge [9], while the soft-particle model was validated in the frictionless case of Walton and Braun [10].

III. RESULTS AND DISCUSSION

Prior to making large numbers of stress tensor measurements, parametric studies were conducted on the effect of the simulation time step on the stress results for frictionless systems. These results are presented in Sec. III A, while the stress tensor measurements are presented in Secs. III B and III C.

A. Effect of simulation time step on the measured stress tensor

For a time step of small enough size, the simulation results from any model—including the stress tensor measurements—should be independent of the time step size. However, in the interest of reducing the computational requirements, it is desired to use the largest time step possible that still yields accurate results. To determine the appropriate time step, the stress results were examined as a function of time step for frictionless systems with various solids fractions and coefficients of restitution.

The stresses are plotted in Fig. 2 as a function of the average relative overlap $\langle\delta\rangle/d$ for the hard-particle-with-overlap model for $e_N=0.9$ and $\nu=0.1$ and 0.5. Both the kinetic and collisional contributions to the stress components τ_{xx}, τ_{xy}, and τ_{yy}, are presented. For the hard-particle model, the time step is proportional to the average collisional overlap by

$$\Delta t \sim L/|\mathbf{g}| \sim L/(\dot{\gamma}d) \sim \langle\delta\rangle/(\dot{\gamma}d), \tag{12}$$

where $\mathbf{g}$ is the relative collision velocity vector which scales with $\dot{\gamma}d$. Thus, the average relative overlap $\langle\delta\rangle/d$ scales with the time step Δt. Smaller time steps, corresponding to smaller average collision overlaps, produce stresses that asymptote to the hard-particle, event-driven simulation values. As the average overlap increases, the simulation results become less computationally expensive due to the increased simulation time step, but the measured stresses begin to deviate from the asymptotic values. For a relative error of less than 2.5% in the stress measurements for $e_N=0.9$, the overlap must remain within approximately 1.5% for $\nu=0.05$ and 0.1, 1% for $\nu=0.3$, 0.5% for $\nu=0.5$, and 0.2% for $\nu=0.7$. These guidelines are similar to the results obtained by Hopkins and Louge [9]. The guidelines for $e_N=0.5$ show a trend similar to that for $e_N=0.9$ as illustrated in Fig. 3, but have slightly smaller values at 1.0% overlap for $\nu=0.05$ and 0.1, 0.75%

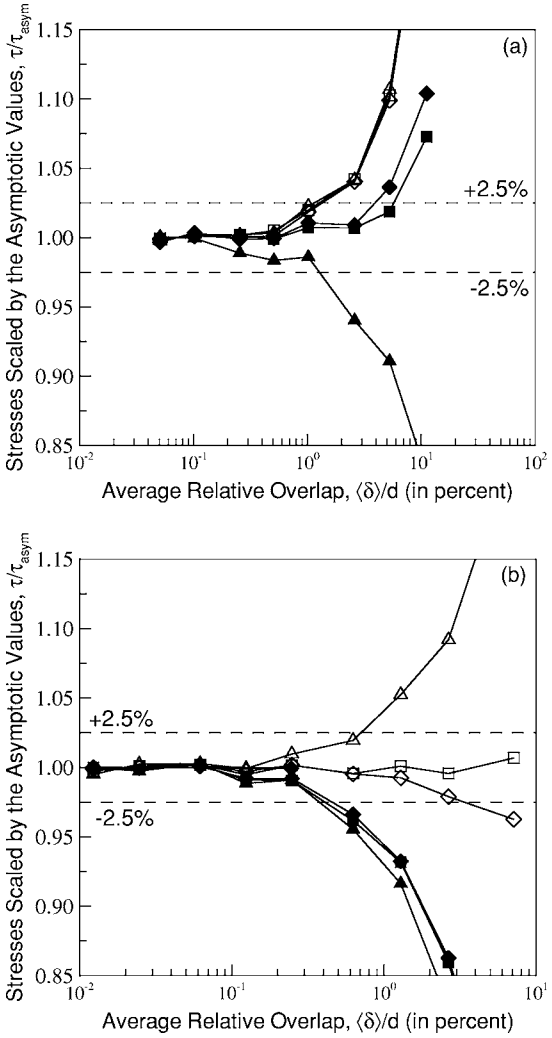

FIG. 2. Stress results from the hard-particle-with-overlap algorithm for e_N=0.9, ν= (a) 0.1 and (b) 0.5. For sufficiently small time steps (Δt is proportional to the relative overlap) the stresses approach an asymptotic value equal to the event-driven hard-particle value. As the time step increases, the error increases. The horizontal lines show relative error thresholds of ±2.5%. Open symbols, kinetic contribution; closed symbols, collisional contribution. Squares, *xx* component; triangles, $-xy$ component; and diamonds, *yy* component.

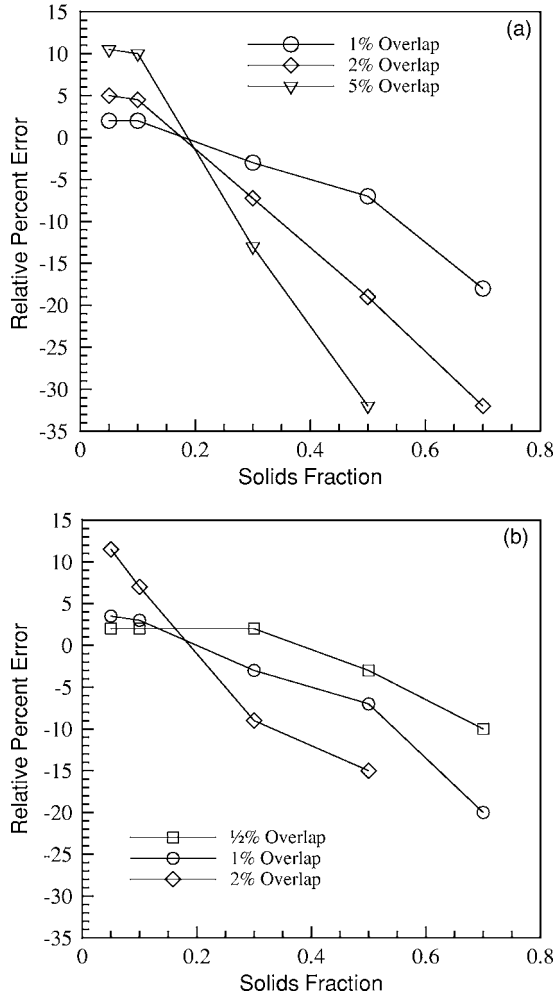

FIG. 3. Percent error in stress results as compared to the asymptotic values (equivalent to the hard-particle, no-overlap results) for the hard-particle-with-overlap model at e_N= (a) 0.9 and (b) 0.5.

for ν=0.3, 0.4% for ν=0.5, and 0.15% for ν=0.7.

In Fig. 4, the stresses are plotted as a function of soft-particle time step for e_N=0.9 and ν=0.1 and 0.5. Here, the time step is scaled by the theoretical binary collision time T_b, which is given by [24]

$$T_b = \sqrt{\frac{m}{2k_U}}\frac{\pi}{2}\left(1+\sqrt{\frac{k_U}{k_L}}\right). \tag{13}$$

Large time steps produce numerical instabilities. However, time steps Δt less than approximately 1/15 of the binary collision contact time T_b produce similar stress results. This cutoff value of $\Delta t \approx T_b/15$ appears to hold for the various solids fractions and loading spring stiffnesses considered in this work. However, at e_N=0.5, time steps of up to approximately $T_b/6$ still produced accurate stress results. In a survey of previous DEM work, the size of time step is often about $T_b/50$ (see, for example, [10,17,18]) and sometimes as large as $T_b/15$ [29].

The results in the following section were obtained using a small enough time step to give asymptotic stress values. For the hard-particle-with-overlap model, the time step was selected so that the overlap guidelines were met. For the soft-particle model, the time step was $T_b/33$ in order to be slightly more conservative than the $T_b/15$ threshold shown in Fig. 4.

B. Stress tensor results for frictionless particles

Figure 5 plots the normal and shear stresses from the soft-particle and hard-particle-with-overlap models as a function of solids fraction ν for e_N=0.9. Both the stresses and the soft-particle loading stiffness are made dimensionless by dividing by $\rho d^2\dot{\gamma}^2$. The dimensionless loading stiffness is subsequently denoted by k_L^*. Also plotted in the figure are the kinetic theory predictions of Jenkins and Richman [30]. The

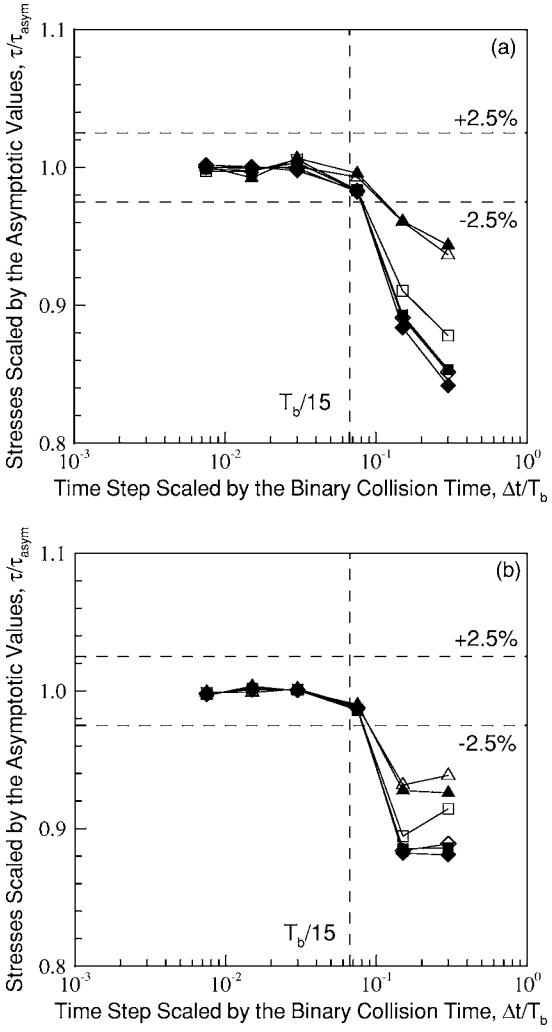

FIG. 4. Stress results from the soft-particle model for $e_N=0.9$ and $k_L/\rho d^2\dot{\gamma}^2=78\,500$, for $\nu=0.1(a)0.1$ and (b) 0.5 as a function of time step size Δt scaled by the theoretical binary collision time T_b. For sufficiently small Δt, the stresses approach an asymptotic value. As the time step increases, the error increases. Symbols as in Fig. 2.

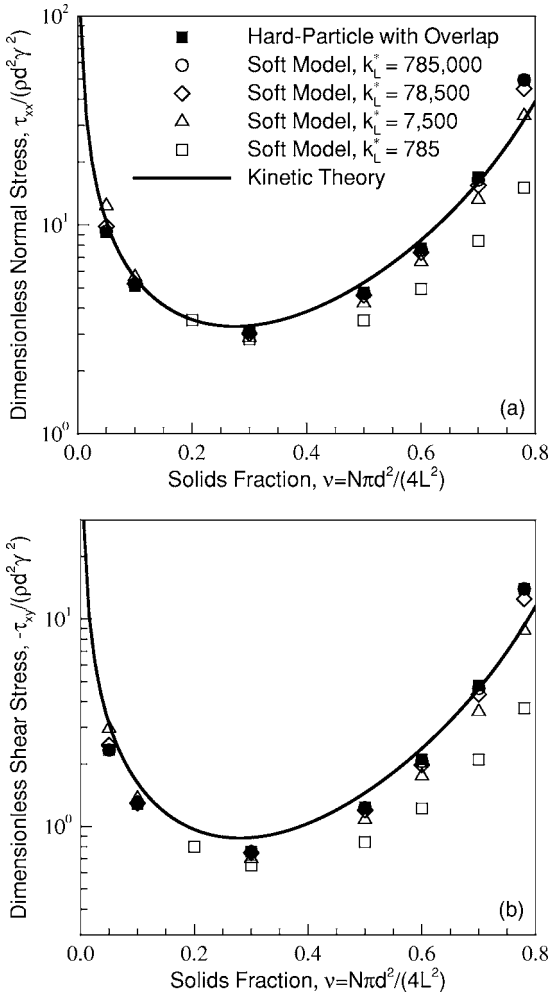

FIG. 5. Dimensionless (a) normal and (b) shear stress results for $e_N=0.9$ from hard-particle-with-overlap and soft-particle simulations for frictionless particles. The kinetic theory predictions of Jenkins and Richman [30] are indicated by the solid lines.

stress results from both models closely match those predicted by kinetic theory for each of the sampled solids fractions. The data from the soft-particle model show that as the loading stiffness increases, the stress measurements asymptotically approach the hard-particle results. For the small loading stiffnesses, the stresses are underpredicted at the large solids fractions. For small solids fractions, however, this trend is reversed and the stresses are slightly overpredicted. This effect is a result of large collisional overlaps which occur while using small loading stiffnesses and will be further explained in the coming paragraphs. Note that no data are plotted for $k_L^*=785$ for $\nu<0.2$, as the particles begin to pass through one another for the smallest stiffnesses and solids fractions. It should be noted here that stiffnesses on the order of $k_L^*=785$ are extremely small and should not be expected to provide accurate results. These results are merely included to help show the trends with varying stiffness magnitudes.

Figure 6 plots the stress data for each model and the kinetic theory for $e_N=0.5$. These plots show results with less variation between models, yet are qualitatively similar to those in Fig. 5. Additionally, the stresses are overpredicted by the kinetic theory at this reduced coefficient of restitution. A subtle difference between Figs. 5 and 6 is shown for the largest solids fractions. For $e_N=0.5$, in Fig. 6, the stress measurements do not show the same increasing trend with loading stiffness at $\nu>0.7$, but rather they appear to overshoot the asymptotic value and approach it from above. This differs from the trend for $e_N=0.9$ where the stresses monotonically increase with loading stiffness at large solids fractions. The cause of this effect is not readily apparent, but does not appear to be due to clustering or system size effects.

The average collisional overlap is strongly dependent on the loading stiffness as shown in Fig. 7 where the average overlap values for the data shown in Fig. 5 are plotted as a function of the loading spring stiffness. Equating the initial impact kinetic energy with the energy stored in the loading spring at maximum deformation demonstrates that for a given shear rate and solid fraction, the relative overlap will vary inversely with the square root of the spring stiffness. The simulation data support this reasoning. Hence, it is im-

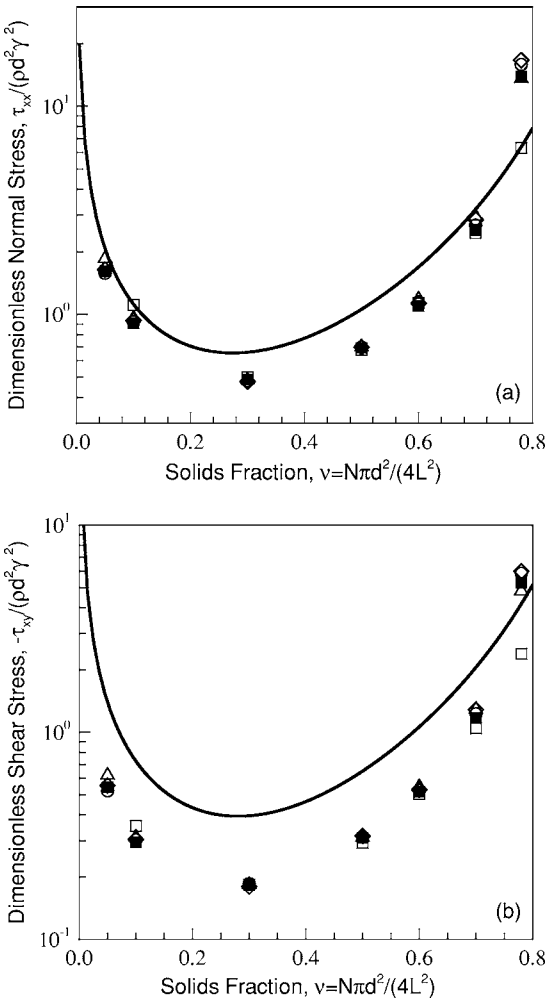

FIG. 6. Dimensionless (a) normal and (b) shear stress results for $e_N=0.5$ from hard-particle-with-overlap and soft-particle simulations for frictionless particles. The kinetic theory predictions of Jenkins and Richman [30] are indicated by the solid lines. Symbols as in Fig. 5.

portant to have a sufficiently stiff spring constant to maintain small average overlaps.

In Fig. 8 the average relative overlaps are shown as a function of solids fraction for a range of soft-particle loading stiffnesses. The average overlap can become quite large at small solids fractions and small loading stiffnesses. No data are included for $k_L^*=785$ at the smallest solids fractions as the overlap becomes so large the particles begin to pass through one another. The large overlaps at small solids fractions are attributed to larger relative impact velocities. At small solids fractions, particles can move in the transverse (y) direction from regions of small mean x velocity into areas of higher mean x velocity, and vice versa. Collisions between particles in these layers will have a large relative impact velocity resulting in a large overlap. The effect of solids fraction on the impact velocity can be estimated from the following simple analysis. The distance a particle travels before impacting another particle, i.e., the mean free path λ, will scale with the particle diameter and be inversely proportional to the solids fraction [31,32]:

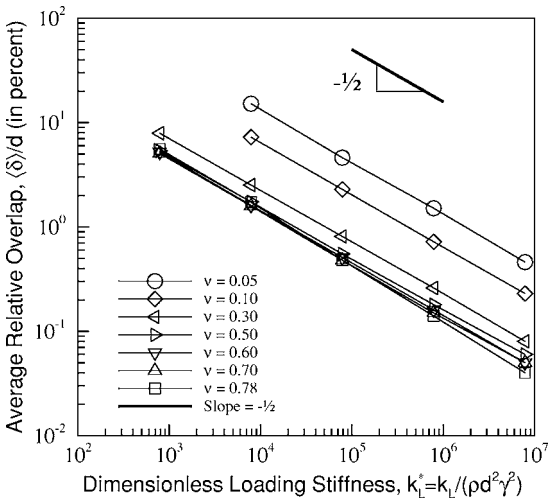

FIG. 7. Average soft-particle relative overlap as a function of the loading spring constant for varying solids fractions at $e_N=0.9$ for frictionless particles.

$$\lambda \sim \frac{d}{\nu}. \tag{14}$$

The relative impact velocity $\mathbf{g}$ of particles from different transverse layers will be the shear rate multiplied by the mean free path:

$$|\mathbf{g}| = \lambda\dot{\gamma} \sim \frac{d\dot{\gamma}}{\nu}. \tag{15}$$

Hence, the relative impact velocity is expected to be proportional to the particle diameter and shear rate, and inversely proportional to the solids fraction. The data in Fig. 8 support this analysis for $\nu<0.5$.

The data in Fig. 8 also indicate that the average overlap begins to increase at the largest solids fractions. This is potentially due to the formation of force chains [33]. Figure 9

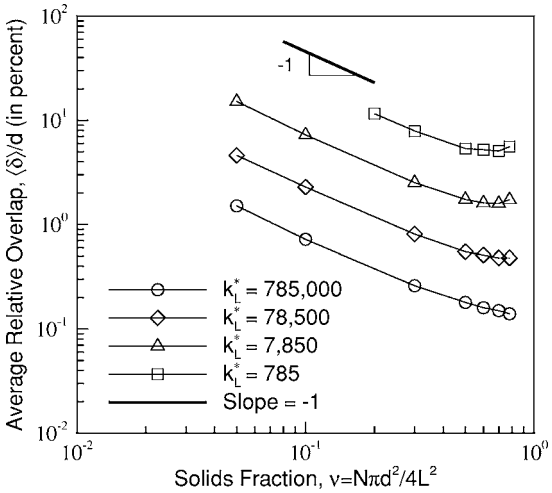

FIG. 8. Average relative overlap for soft-particle collisions as a function of system solids fraction for the given loading spring stiffnesses and frictionless particles at $e_N=0.9$.

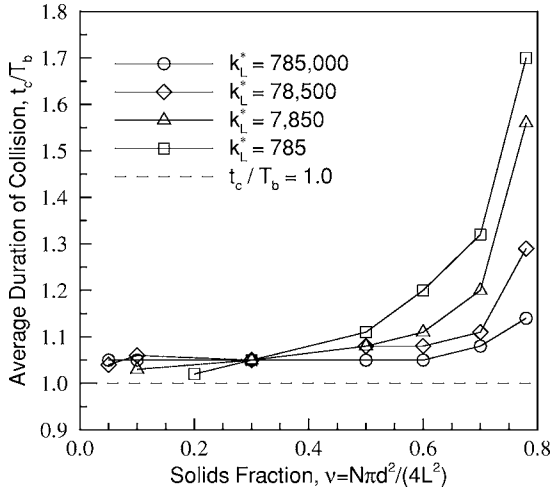

FIG. 9. Average particle contact time t_c scaled by the theoretical binary contact time T_b for the soft-particle model as a function of solids fraction for the given loading spring stiffnesses and frictionless particles at $e_N=0.9$.

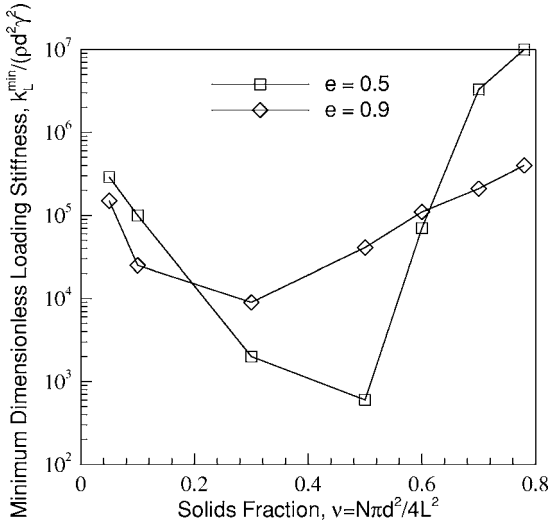

FIG. 10. Minimum dimensionless loading stiffness for the soft-particle model as a function of solids fraction for frictionless particles and $e_N=0.5$ and 0.9. Using stiffnesses larger than this minimum will ensure that stress results are within ±2.5% error from the respective asymptotic values.

plots the average contact time t_c scaled by T_b, as a function of solids fraction. An average contact time of $t_c/T_b=1$ indicates the flow is purely collisional and consists solely of binary collisions. Values slightly above 1 indicate that some longer-lasting collisions exist, although the flow may still be described as collisional [18]. For $\nu>0.7$, the average collision time increases sharply. These long-lasting contacts signify that the flow is noncollisional and consists of particles in force chains. This causes the average overlap to increase at the largest solids fractions as shown in Fig. 8. Figure 9 shows that this transition begins at smaller solids fractions for smaller values of the spring stiffness.

The data in Figs. 5 and 6 make it clear that loading stiffness must be sufficiently large to obtain asymptotic stress measurements that approach the hard-particle predictions. Additionally, the preceding discussion demonstrates that collisional overlap is an important variable in soft-particle modeling. By plotting the stress measurements as a function of loading stiffness, it is possible to determine a minimum stiffness above which the stress results vary by less than ±2.5%. These minimum loading stiffnesses are summarized in Fig. 10 for each solids fraction and coefficient of restitution. For either small or large solids fractions, relatively large stiffnesses are required to maintain small values of collisional overlap, and thus asymptotic stress results. But, for moderate solids fractions, a smaller stiffness will still yield accurate results. The stiffness must be large at small solids fractions because overlap quickly increases for the large relative velocity collisions that occur at small solids fractions (see Fig. 8). For large solids fractions, the stiffness must also be large because the dependence of stresses on overlap is intensified by the large solids fraction.

The deviation in the stress measurements at small stiffnesses shown in Figs. 5 and 6 is caused by the large variation in overlap shown in Figs. 7 and 8. This effect of overlap can be circumvented to some degree by considering the effective particle diameter d_{eff}, which is given by

$$d_{eff} = d - \langle \delta \rangle, \tag{16}$$

where $\langle \delta \rangle$ is the average collisional overlap, $0<\langle \delta \rangle<d$. For conditions resulting in large overlaps, the effective particle diameter can be significantly smaller than the true diameter. This smaller effective diameter in turn leads to a smaller effective solids fraction ν_{eff}:

$$\nu_{eff} = \frac{N\pi(d-\langle \delta \rangle)^2}{4L^2}. \tag{17}$$

By plotting the stress measurements of Fig. 5(a) as a function of the *effective* solids fraction, as shown in Fig. 11, the data for the smaller loading stiffnesses are shifted to the left and much more closely follow the trend of both the hard-particle-with-overlap model and the soft-particle model with the largest loading stiffnesses. This could potentially be used as a time saving feature in future DEM modeling efforts. One could use an artificially small loading stiffness in order to use a larger time step by simply making a corresponding increase to the particle size.

C. Stress tensor results for frictional particles

Figure 12 plots the normal stresses from the soft-particle and hard-particle-with-overlap models as a function of solids fraction ν for frictional particles with $\mu=0.5$ and $e_N=0.9$. The stresses show an overall decrease in magnitude as compared to the frictionless case shown in Fig. 5(a). This is attributed to the addition of frictional dissipation and the shift of some kinetic energy from translational to rotational modes. Each of these changes causes a reduction in both fluctuating velocities and collisional forces, thereby leading to reduced stress magnitudes.

Two other observations can also be made from the data in Fig. 12. First, there is a diminished dependence on the spring

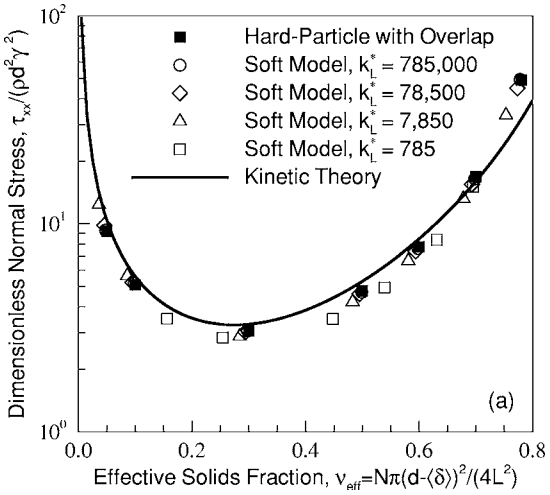

FIG. 11. Dimensionless normal stresses for $e_N=0.9$ [same data as in Fig. 5(a)] as a function of the *effective* solids fraction [Eq. (17)]. The use of this effective solids fraction accounts for the differences in collisional overlap resulting from different loading stiffnesses. Thus, the soft-particle results for small loading stiffnesses more closely follow the trend for large loading stiffnesses.

stiffness for the frictional case. Second, at the largest solids fraction, as the spring stiffness increases, the stresses overshoot and then come back to the asymptotic value. Both of these effects were also seen in the frictionless case for $e_N=0.5$ in Fig. 6. Thus, these effects appear for systems with significant collisional dissipation, regardless if it is due to inelasticity or friction. Results presented by Babić *et al.* [17] also show this overshoot for solids fractions of 0.70 and 0.75 for $\mu=0.5$ and $e_N=0.8$. They attributed this overshoot to potential statistical uncertainties. The present results seem to indicate that the overshoot in stresses may be due to more than simple statistical uncertainty, as the average stress values show the overshoot. A possible cause may be due to the competing effects of the effective solids fraction (stresses increasing with spring stiffness) and an effect of average contact time (average contact time and stresses decrease with

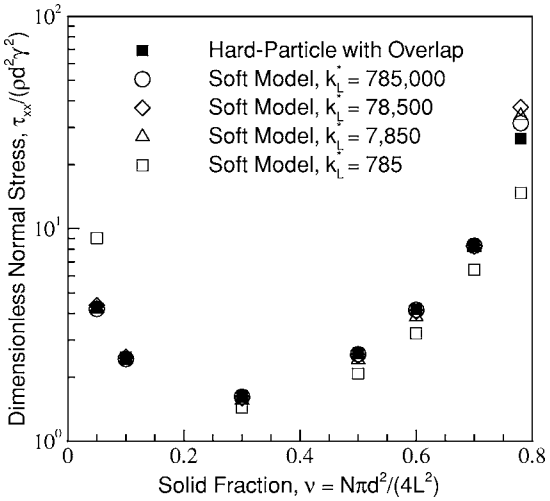

FIG. 12. Dimensionless normal stress results for frictional particles with $\mu=0.5$ and $e_N=0.9$.

increasing spring stiffness) that does not show up for the nearly elastic, frictionless case.

Large fluctuations between window averaged stress measurements over time are observed in the present results as shown in Fig. 13(a). These fluctuations are greater for frictional systems as compared to frictionless systems, and this increase in fluctuation magnitude is attributed to changes in granular structure as shown in Figs. 13(b) and 13(c). The granular structure tends to be in either a semiordered state with slip planes oriented in the streamwise direction or in a more random structure without these streamwise planes present. When the streamwise planes are present, Fig. 13(b), the stresses are near a minimum value. The structure may change such that these slip planes do not exist or are not oriented in the streamwise direction, Fig. 13(c), at which point for frictional particles, long, diagonally oriented force chains form which lead to a sharp increase in stresses. The shading of each particle in Figs. 13(b) and 13(c) is proportional to the instantaneous force acting on each particle, where darker shades indicate larger forces. The particle shading in Fig. 13(c) makes the formation of force chains very apparent. In contrast, for the frictionless case, when the slip planes are not oriented in the streamwise direction, the particles are able to still move past one another without the formation of extensive force chains and the corresponding sharp increase in stresses.

The data for frictional particles with $\mu=0.5$ and $e_N=0.5$ also show good agreement between models, little dependence on the spring stiffness for moderate solids fractions, overshoot of stresses for $\nu=0.78$, and an overall decrease in the magnitude of the stresses as compared to Figs. 6 and 12.

The stress results for intermediate values of the friction coefficients and $e_N=0.9$ are shown in Fig. 14. With the addition of a small amount of friction, the stresses are significantly reduced. These results also show the extent to which the stresses become nearly invariant with the examined spring stiffnesses for highly frictional particles.

IV. CONCLUSIONS

This work shows that accurate stress results are obtained by both hard-particle-with-overlap and soft-particle approaches over a wide range of solids fractions, for two different coefficients of restitution, and for the frictionless and frictional particles examined herein. The stresses from the soft-particle model begin to show increasing deviation as the loading stiffness decreases, but with a sufficiently large loading stiffness, the soft-particle model asymptotes to the hard-particle predictions. The value of spring stiffness which may be deemed "sufficiently large" varies with solid fraction and coefficient of restitution. Relatively large loading stiffnesses are required for systems with solids fractions near the high or low extremes. Smaller loading stiffnesses may be used for systems with moderate solids fractions.

For frictional particles, good agreement between the models is also obtained. Additionally, the magnitude of stresses decreases with the addition of friction and the stresses become relatively insensitive to spring stiffness for large friction coefficients.

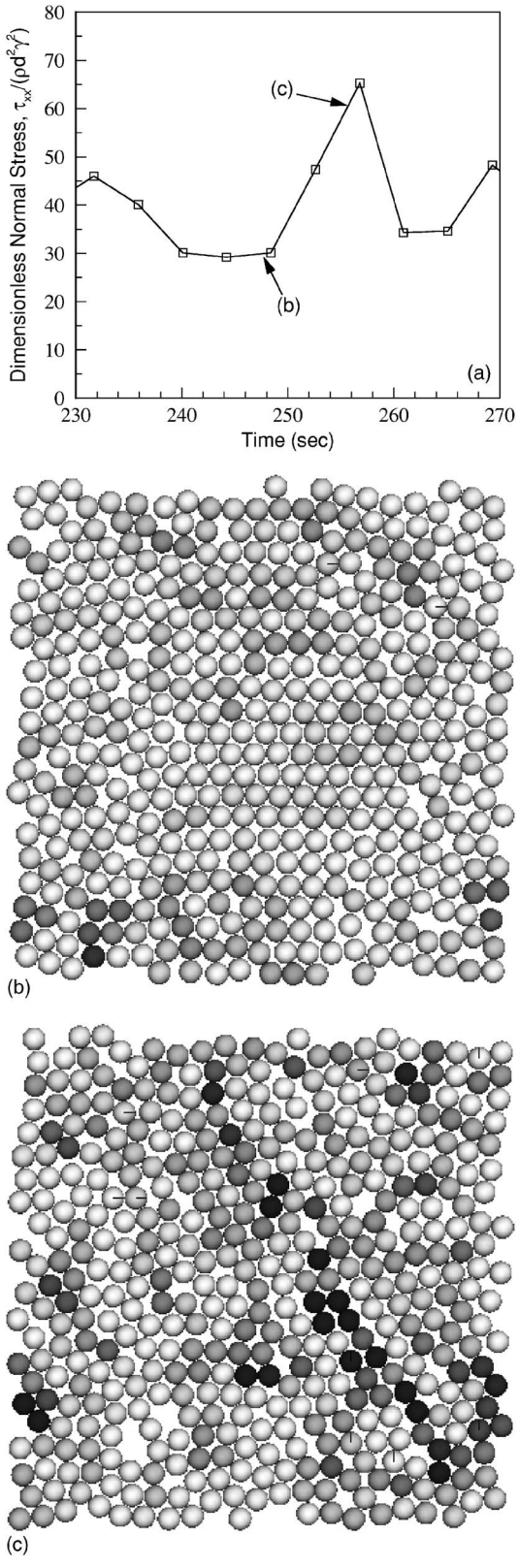

FIG. 13. (a) Dimensionless normal stress window averages over simulation time for $\nu=0.78, e_N=0.9, \mu=0.5$, and $k_L^*=78\,500$; snapshot of the granular structure at (b) a small stress state, $\Theta\simeq 248$ s and (c) a large stress state, $\Theta\simeq 256$ s. The shading of each particle is proportional to the instantaneous force acting on that particle, where darker shades indicate larger forces.

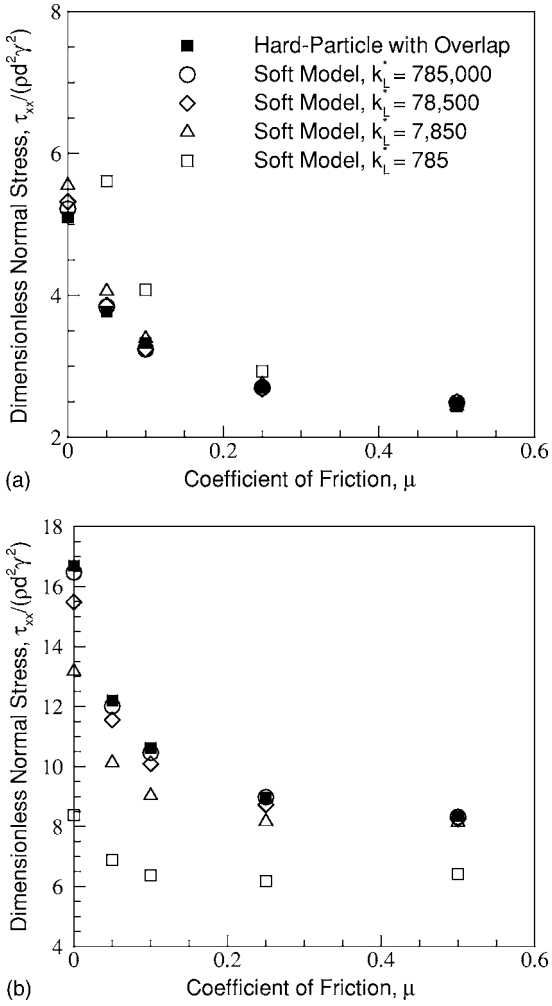

FIG. 14. Dimensionless normal stresses for $e_N=0.9$ as a function of friction coefficient for $\nu=$ (a) 0.1 and (b) 0.7.

Accurate stress results are also dependent on proper selection of the time step. Increasing the simulation time step results in improved computation times, but at the expense of accuracy. Determination of the proper time step is a straightforward process using the parametric studies described previously. For the soft-particle model, the time step must be small enough for the integration scheme to yield accurate results. Parametric studies show that a time step of $T_b/15$ produces satisfactory results, but a more conservative time step of $T_b/33$ was used for all of the present simulations. For the hard-particle-with-overlap model, too large of a time step can cause large overlaps and, if the overlaps are large enough, result in erroneous stress measurements. The stress results and overlap threshold are in agreement with previous work [9].

The results presented here indicate that for a dilute granular shear flow, each of the three tested models predicts similar flow stresses that also agree well with those predicted by kinetic theory. From the standpoint of accuracy, there does not seem to be any certain set of conditions for which one model outperforms another. Selection of a contact algorithm then appears to be primarily based on how the computation speed of the algorithm scales with the system size.

[1] T. G. Drake, J. Fluid Mech. **225**, 121 (1991).
[2] L. Bocuet, W. Losert, D. Schalk, T. C. Lubensky, and J. P. Gollub, Phys. Rev. E **65**, 011307 (2001).
[3] D. M. Mueth, Phys. Rev. E **67**, 011304 (2003).
[4] G. D. R. Midi, Eur. Phys. J. E **14**, 341 (2004).
[5] G. I. Tardos, S. McNamara, and I. Talu, Powder Technol. **131**, 23 (2003).
[6] T. G. Drake and O. R. Walton, J. Appl. Mech. **71**, 597 (1995).
[7] M. Lätzel, S. Luding, H. J. Herrmann, D. W. Howell, and R. P Behringer, Eur. Phys. J. E **11**, 325 (2003).
[8] C. S. Campbell and A. Gong, J. Fluid Mech. **164**, 107 (1986).
[9] M. A. Hopkins and M. Y. Louge, Phys. Fluids A **3**, 47 (1991).
[10] O. R. Walton and R. L. Braun, J. Rheol. **30**, 949 (1986).
[11] C. S. Campbell, J. Fluid Mech. **203**, 449 (1989).
[12] C. S. Campbell and C. Brennen, J. Fluid Mech. **151**, 167 (1985).
[13] E. D. Liss and B. J. Glasser, Powder Technol. **116**, 116 (2001).
[14] M. E. Lasinski, J. S. Curtis, and J. F. Pekny, Phys. Fluids **16**, 265 (2004).
[15] M. L. Tan and I. Goldhirsch, Phys. Fluids **9**, 856 (1997).
[16] P. A. Cundall and O. D. L. Strack, Geotechnique **29**, 47 (1979).
[17] M. Babić, H. H. Shen, and H. T. Shen, J. Fluid Mech. **219**, 81 (1990).
[18] C. S. Campbell, J. Fluid Mech. **465**, 261 (2002).
[19] M. A. Hopkins, Department of Civil and Environmental Engineering Report No. 87-7, Clarkson University, Potsdam, New York, 1987 (unpublished).
[20] M. Y. Louge, Phys. Fluids **6**, 2253 (1994).
[21] C. S. Campbell, in *Proceedings of the Tenth U.S. National Congress of Applied Mechanics, Austin, 1986* (unpublished), p. 327.
[22] A. W. Lees and S. F. Edwards, J. Phys. C **5**, 1921 (1972).
[23] J. Schäfer, S. Dippel, and D. E. Wolf, J. Phys. I **6**, 5 (1996).
[24] S. Luding, in *Physics of Dry Granular Media*, edited by H. J. Herrmann, J.-P. Hovi, and S. Luding (Kluwer Academic Publishers, Dordrecht, 1998).
[25] H. J. Herrmann and S. Luding, Continuum Mech. Thermodyn. **10**, 189 (1998).
[26] P. K. Haff and B. T. Werner, Powder Technol. **48**, 239 (1986).
[27] J. Schäfer and D. E. Wolf, Phys. Rev. E **51**, 6154 (1995).
[28] F. Radjai, J. Schäfer, S. Dippel, and D. Wolf, J. Phys. I **7**, 1053 (1997).
[29] C. M. Dury and G. H. Ristow, J. Phys. I **7**, 737 (1997).
[30] J. T. Jenkins and M. W. Richman, Phys. Fluids **28**, 3485 (1985).
[31] H. W. Liepmann and A. Roshko, *Elements of Gas Dynamics* (Wiley, New York, 1957).
[32] C. R. Wassgren, J. A. Cordova, R. Zenit, and A. Karion, Phys. Fluids **15**, 3318 (2003).
[33] D. Howell, R. P. Behringer, and C. Veje, Phys. Rev. Lett. **82**, 5241 (1999).